CrossMark

Effects of Geometries and Substructures of ICMEs on Geomagnetic Storms

Jae-Ok Lee[1] · **Kyung-Suk Cho[1,2]** · **Rok-Soon Kim[1,2]** ·
Soojeong Jang[3] · **Katsuhide Marubashi[4]**

Abstract To better understand geomagnetic storm generations by ICMEs, we consider the effect of substructures (magnetic cloud, MC, and sheath) and geometries (impact location of flux-rope at the Earth) of the ICMEs. We apply the toroidal magnetic flux-rope model to 59 CDAW CME–ICME pairs to identify their substructures and geometries, and select 20 MC-associated and five sheath-associated storm events. We investigate the relationship between the storm strength indicated by minimum Dst index (Dst_{min}) and solar wind conditions related to a southward magnetic field. We find that all slopes of linear regression lines for sheath-storm events are steeper (≥ 1.4) than those of the MC-storm events in the relationship between Dst_{min} and solar wind conditions, implying that the efficiency of sheath for the process of geomagnetic storm generations is higher than that of MC. These results suggest that different general solar wind conditions (sheaths have a higher density, dynamic and thermal pressures with a higher fluctuation of the parameters and higher magnetic fields than MCs) have different impact on storm generation. Regarding the geometric encounter of ICMEs, 100% (2/2) of major storms ($Dst_{min} \leq -100$ nT) occur in the regions at negative P_Y (relative position of the Earth trajectory from the ICME axis in the Y component of the GSE coordinate) when the eastern flanks of ICMEs encounter the Earth. We find similar statistical trends in solar wind conditions, suggesting that the dependence of geomagnetic storms on 3D ICME–Earth impact geometries is caused by asymmetric distributions of the geoeffective solar wind conditions. For western flank events, 80% (4/5) of the major storms occur in positive P_Y regions, while intense geoeffective solar wind conditions are not located in the positive P_Y. These results suggest that the strength of geomagnetic storms depends on ICME–Earth impact geometries as they determine the solar wind conditions at Earth.

✉ J.-O. Lee
ljoking@kasi.re.kr

[1] Korea Astronomy and Space Science Institute, Daejeon, 34055, Korea

[2] University of Science and Technology, Daejeon, 34055, Korea

[3] School of Space Research, Kyung Hee University, Yongin, 17104, Korea

[4] Asia Space Environment Research Consortium, Tokyo, 182-0024, Japan

1. Introduction

A geomagnetic storm is a temporary and major disturbance of the Earth's magnetic field and its physical processes can be summarized as follows: 1) the southward magnetic field (B_S) of solar wind reconnects with the geomagnetic field near the dayside of the magnetosphere, which leads to an energy transfer from mechanical solar wind energy to magnetic energy stored in the magnetotail; 2) the enhanced magnetic energy causes an increase in magnetospheric electric currents; and 3) these electric currents produce magnetic disturbances on the Earth (Dungey, 1961; Gonzalez *et al.*, 1994). The geomagnetic storm can adversely influence electric power, navigation, and communication systems as well as spacecraft operations. One measure of geomagnetic storm activity is the disturbance storm time (Dst) index that represents magnetic disturbances caused by westward equatorial electrojets, known as ring currents, which lead to decreases in geomagnetic fields. The Dst index is based on measurements of the horizontal component of the geomagnetic fields from four magnetometers near the equator (Sugiura and Kamei, 1991). Based on the minimum value of the hourly Dst index (Dst_{min}), geomagnetic storms are classified as follows: weak storm ($Dst_{min} > -50$ nT), moderate storm (-50 nT $\geq Dst_{min} > -100$ nT), intense storm (-100 nT $\geq Dst_{min} > -200$ nT), and super intense storm ($Dst_{min} \leq -200$ nT) (Gonzalez *et al.*, 1994; Kim *et al.*, 2010; Lee *et al.*, 2014).

Coronal mass ejections (CMEs) belong to the most explosive phenomena in the solar corona that expel massive amounts of coronal material and magnetic fields into interplanetary space. These CMEs and their associated shocks (CME-driven shocks) can be detected in interplanetary space where they are known as interplanetary CMEs (ICMEs) and their associated shocks (ICME-driven shocks), which are the key drivers of major geomagnetic storms ($Dst_{min} \leq -100$ nT) (Gonzalez *et al.*, 2007; Zhang *et al.*, 2007; Echer *et al.*, 2008; Richardson and Cane, 2012). CME- and ICME-driven shocks are generated by fast CMEs and ICMEs whose speeds exceed fast-mode magnetosonic speeds. ICMEs are observed by *in situ* solar wind plasma and magnetic field detectors such as the *Advanced Composition Explorer* (ACE), *Wind*, and *Solar Terrestrial Relations Observatory* (STEREO).

By examining solar wind and interplanetary magnetic field data, several researchers divided the structure of ICMEs into three parts, according to the observational signatures (Burlaga *et al.*, 1981; Klein and Burlaga, 1982; Zhang *et al.*, 2007; Richardson and Cane, 2010): 1) an ICME-driven shock defined by the sudden enhancement of solar wind speed and density; 2) a sheath defined by enhanced and fluctuating magnetic field strength; and 3) a magnetic cloud (MC) defined by the signature of a rotating magnetic field in a north–southward magnetic field component (B_Z) and low beta plasma or low proton temperature (or ejecta defined by no signature of a rotating magnetic field). Some researchers occasionally classified the MC structures into several types according to both flux-rope orientations with respect to the ecliptic plane and their leading and trailing magnetic field polarities: 1) high-inclination, East–West and West–East type clouds; and 2) low-inclination, North–South and South–North type clouds (Zhao and Hoeksema, 1996; Bothmer and Rust, 1997; Mulligan, Russell, and Luhmann, 1998). For example, North–South type clouds indicate that B_Z of MCs rotates from northward to southward.

A number of studies have investigated the interplanetary origins in each of the strong or weak geomagnetic storms, depending on their strength during Solar Cycle 23 (Zhang *et al.*,

2007; Echer *et al.*, 2008; Gonzalez *et al.*, 2011; Richardson and Cane, 2012; Echer, Tsurutani, and Gonzalez, 2013). For major storms, ICMEs are dominant drivers: 87% (77/88) by Zhang *et al.* (2007) and 79% (71/90) by Echer *et al.* (2008). The remainder is made up of corotating interaction regions (CIRs) by interactions between fast and slow solar wind streams, the heliospheric current sheet (HCS), and complex structures by interactions between ICMEs (see Echer *et al.*, 2008 for details). For moderate storms, 48% (102/213) and 20% (44/213) are related to CIRs and ICMEs, respectively (Echer, Tsurutani, and Gonzalez, 2013).

To determine the geoeffective solar wind parameters of ICMEs, many studies have appeared quantifying the relationships between Dst_{min} and solar wind conditions of ICMEs, such as the minimum value of B_S (B_{Smin}), the maximum solar wind speed (V_{max}) (or mean solar wind speed (V_{mean})), and convection electric fields ($E_{Y_{V_{max}}} = V_{max} \times B_{Smin}$ or $E_{Y_{V_{mean}}} = V_{mean} \times B_{Smin}$) (Echer *et al.*, 2008; Gopalswamy, 2008; Richardson and Cane, 2010, 2012). Here, ICMEs indicate MCs and/or sheaths. By analyzing 300 ICME–storm pairs from 1996 to 2009, Richardson and Cane (2010) found that the southward magnetic field and electric field in ICMEs have higher correlation coefficients (CC) with the Dst_{min} than the solar wind speed: CC = 0.89 for B_{Smin}, CC = 0.90 for $E_{Y_{V_{max}}}$, and CC = −0.54 for V_{max}. Here, the meaning of CC = −0.54 for V_{max} is that the Dst index decreases as the solar wind speed increases, implying that a fast solar wind is more geoeffective than a slow solar wind. Several researchers have investigated the dependence of geomagnetic storms on the geoeffective ICME substructures (Huttunen and Koskinen, 2004; Gopalswamy, 2008; Yermolaev *et al.*, 2010, 2012). Here, the geoeffective ICME substructures generally can be classified into two groups: MC-associated and sheath-associated storm events, which indicate that Dst_{min} is mainly caused by southward magnetic fields of MCs and sheaths, respectively. By examining 50 MC-storms and 59 sheath-storms, Gopalswamy (2008) found that correlation coefficients of solar wind conditions in MCs with Dst index are similar to those in sheaths: in MC-storm (sheath-storm) events, CC = −0.65 (−0.67) for V_{mean}, CC = 0.79 (0.77) for B_{Smin}, and CC = 0.90 (0.86) for $E_{Y_{V_{mean}}}$.

Since the development of two fitting techniques (linear force-free cylindrical and toroidal flux-rope models) to determine three-dimensional (3D) magnetic field structures and geometries of ICMEs with MCs (Marubashi and Lepping, 2007), several researchers examined magnetic and geometrical relationships between ICMEs and their solar sources (Marubashi *et al.*, 2012; Cho *et al.*, 2013, 2017; Marubashi *et al.*, 2015). Here the fitting techniques assumed that the global structures of ICMEs are loops extending from the Sun with both legs rooted on the solar surface, and the internal magnetic field structures are helical flux ropes (Goldstein, 1983; Marubashi, 1986; Burlaga, 1988; Lepping, Burlaga, and Jones, 1990; Bothmer and Schwenn, 1998). The main difference between the toroidal model and the cylindrical model is whether or not the curvature effects of ICMEs can be taken into account to explain the observed magnetic field variations. Cho *et al.* (2013) found that 88% (30/34) of the helicity signs of ICMEs are consistent with those of the injected helicities in CME source regions. Marubashi *et al.* (2015) also found that main axis orientations of ICMEs are close to those of the magnetic polarity inversion line in the solar source regions within 25 degrees. Recently, a few studies have attempted to explain causes of geomagnetic storms by investigating the 3D magnetic field structures and geometries of MCs (Marubashi *et al.*, 2016; Cho *et al.*, 2017). Cho *et al.* (2017) examined two ICME–storm pairs and suggested that even if an ICME flank hits the Earth, it can cause a strong storm when its inherent magnetic field keeps southward throughout its passage.

Although many studies have been carried out on the relationship between geomagnetic storms and solar wind conditions of ICMEs, there has been no comprehensive investigation on relationship between geomagnetic storms and geometries of ICMEs. The main purpose

of this study is to find the geometric effects of ICMEs on geomagnetic storms as well as the dependence of geomagnetic storms on ICME substructures. For this purpose, we use 25 ICMEs selected from the 59 events of the Coordinated Data Analysis Workshop (CDAW) ICME list,[1] which are well defined by the toroidal fitting results and have clear geomagnetic storm associations.

This paper is organized as follows. In Section 2, we describe the data selection and analysis. Result and discussion are given in Section 3. A brief summary and conclusion are presented in Section 4.

2. Data and Analysis

2.1. Data

For data selection, we use the following procedure: 1) we consider 59 CME–ICME pairs from the CDAW list, which are selected from the list of 222 shock-driving ICMEs from 1997 to 2006 in Gopalswamy *et al.* (2010) with the following condition: longitudes of CME source regions are near the solar disk center (E15° ≤ source longitude ≤ W15°); and 2) we select 25 events that satisfy the following criteria.

First, they are well fitted by the toroidal fitting model. The meaning of this is as follows. 1) The estimated error value defined as the root mean square (rms) difference between observed and calculated fields divided by the highest observed field intensity is less than 0.3. 2) The difference between the orientations of MC axes determined by the toroidal fitting model and the orientations of polarity inversion lines of their associated solar source regions is less than 30 degree. For the latter feature we assume that ICMEs expand and propagate through the interplanetary space with their orientation maintained (Marubashi and Lepping, 2007; Marubashi *et al.*, 2012, 2015).

Second, their associated geomagnetic storms are well identified, by which we mean that southward magnetic fields of ICMEs lead to geomagnetic storms, which are confirmed by visual inspection of the associations that geomagnetic storms, the minimum values of Dst index, occur within 6 hours of the ICMEs' minimum southward magnetic fields. It should be noted that event selection bias might exist because we used the selection procedure to get our data set (25 events among 59 CME–ICME pairs) and the exclusion of the subset (34 events among 59 CME–ICME pairs), might influence the statistical significance and results. The shock arrival times, start and end times of 25 ICMEs as well as 3D geometrical parameters derived from the toroidal fitting model are listed in Table A1 and A2 in the Electronic Supplementary Material of Marubashi *et al.* (2015). Solar wind data during their passage are obtained from ACE science center[2] for ACE spacecraft data and Coordinated Data Analysis Web (CDAWeb) database[3] for *Wind* spacecraft data. The time resolutions of the ACE and *Wind* data used are 64 and 60 seconds, respectively. We use plasma and magnetic field data expressed in Geocentric Solar Magnetospheric (GSM) coordinate systems.

To determine the strength of geomagnetic storms we use the Dst index, which is provided by the World Data Center.[4] For the selected events, we determine the minimum values of Dst indices (Dst_{min}) caused by the ICMEs and their solar wind conditions: 1) minimum B_S (B_{Smin}), 2) solar wind speed (V_{SW}) at B_{Smin} ($V_{B_{Smin}}$), 3) southward magnetic field duration


(T_{B_S}), which is calculated by sum of time periods during southward magnetic field ($B_Z < 0$), 4) maximum convection electric field ($E_{Y_{B_{Smin}}} = V_{B_{Smin}} \times B_{Smin}$), and 5) solar wind energy proxy ($\int V_{SW} \times B_S \, dt$), which is calculated by time integral of electric field when $B_Z < 0$.

We also determine impact locations of the ICMEs at the Earth by using the 3D geometrical parameters such as the latitude and longitude angles of a vector normal to an ICME plane defined by the axial magnetic field with radius of curvature and thickness of the ICME. Here, the impact location indicates which flank of an ICME encounters the Earth. If the eastern (western) flanks of ICMEs encounter the Earth, we define these events as eastern (western) flank events.

Since there are significant differences in solar wind properties and efficiencies of the generation of magnetic storms between MCs and sheaths (Huttunen and Koskinen, 2004; Gopalswamy, 2008; Yermolaev *et al.*, 2010), we classify 25 ICME–storm pairs into two groups according to the ICME substructures: 20 MC-associated storm events and five sheath-associated storm events. Here, we have MC-associated and sheath-associated storm events, which indicate that Dst$_{min}$ is mainly caused by southward magnetic fields of MCs and sheaths, respectively.

Figure 1 shows examples of MC-associated (upper panels) and sheath-associated (lower panels) storm events. As shown in the upper panels of Figure 1, an ICME-driven shock arrived at 19:13 UT on 18 May 2002 (event No. 17 in Table 1), indicated by the vertical black dashed line. The ICME has a rotating magnetic field in B_Z (hereafter an MC) that was observed by the ACE spacecraft from 02:45 UT on 19 May to 04:45 UT on 20 May, represented by the vertical blue dashed and dot-dashed lines. During the MC passage, southward magnetic fields decrease to a minimum of -12.3 nT at 03:51 UT on 19 May, which resulted in a moderate geomagnetic storm (-58 nT) at 07:00 UT on 19 May. We define this kind of event as an MC-associated storm event because southward magnetic fields of the MC lead to the geomagnetic storm. The solar wind conditions of this ICME are $B_{Smin} = -12.3$ nT, $V_{B_{Smin}} = 471.4$ km s^{-1}, $T_{B_S} = 5.2$ hr, $E_{Y_{B_{Smin}}} = -5.8$ mV m, and $\int V_{SW} \times B_S \, dt = -4.9$ V m s. As shown in the lower panels of Figure 1, an ICME-driven shock arrived at 13:15 UT on 11 April 2001 and a sheath is observed by ACE spacecraft from 13:15 UT to 23:00 UT on 11 April (event No. 13 in Table 1), indicated by vertical black dashed and dot-dashed lines. During the sheath passage, southward magnetic field decreases to a minimum of ~ -33.4 nT at 15:42 UT on 11 April and the magnetic field falls below -10 nT during the period from 20:12 UT to 21:49 UT on 11 April. These conditions produce a super intense geomagnetic storm (-271 nT) at 00:00 UT on 12 April. We define this kind of event as a sheath-associated storm event because southward magnetic fields of the sheath lead to the geomagnetic storm. Solar wind conditions of this ICME are: $B_{Smin} = -33.4$ nT, $V_{B_{Smin}} = 756.2$ km s^{-1}, $T_{B_S} = 6.0$ hr, $E_{Y_{B_{Smin}}} = -25.3$ mV m, and $\int V_{SW} \times B_S \, dt = -17.7$ V m s. These parameters of 25 ICMEs and their associated geomagnetic storms are presented in columns $7-12$ of Table 1.

We also determine impact locations of ICMEs at the Earth by using 3D geometrical parameters from the toroidal fitting model. Here, the 3D geometrical parameters such as radius of curvature and thickness of an ICME as well as relative position of the spacecraft (or Earth) trajectory from an ICME axis in the $Y-Z$ plane of geocentric solar ecliptic (GSE) coordinate system are shown in columns $2-8$ of Table 2, and these parameters are used to estimate 3D ICME–Earth impact geometries. Figure 2 shows 3D geometries of ICMEs (event No. 3 and 6 in Table 1) at the time of encounter with the spacecraft. As shown in the left panel of Figure 2, the eastern flank of the ICME with left-handed magnetic helicity impacts the spacecraft. We define this kind of event as an eastern flank event. In the right panel of Figure 2, the western flank of the ICME having-right handed magnetic helicity im-
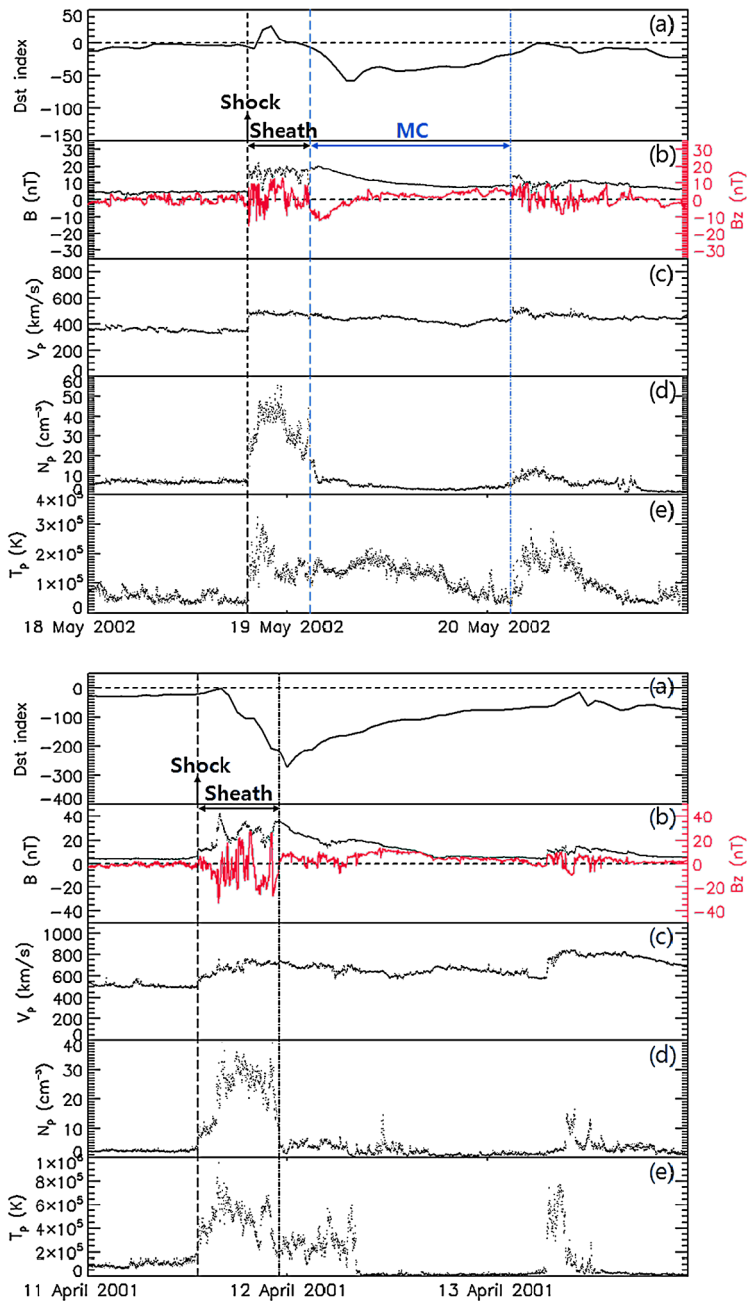
Figure 1   Temporal profiles of geomagnetic disturbances and interplanetary data observed on 18–20 May 2002 (*upper*, event No. 17 in Table 1) and 11–13 April 2001 (*lower*, event No. 13 in Table 1) by the ACE spacecraft. In both diagrams, panels from *top* to *bottom* show the Dst index (**a**), the total magnetic field and southward magnetic field (**b**), the solar wind speed (**c**), the proton number density (**d**), and the proton temperature (**e**). The *vertical black dashed*, *blue dashed* and *dot-dashed lines* represent the shock arrival time, start and end times of MCs, respectively. In the lower panels, the *vertical black dot-dashed line* indicates the end time of a sheath region.

Table 1 Observational solar wind conditions of 25 ICMEs and their associated geomagnetic storms.

Event	ICME shock year/mon/day UT	MC or sheath start mon/day UT	MC or sheath end mon/day UT	Type	S/C	B_{Smin} (nT)	V_{BSmin} (km s^{-1})	T_{BS} (hour)	$E_{Y_{BSmin}}$ (mV m)	$\int V_{SW} \times B_S\, dt$ (V m s)	Dst_{min} (nT)
1	1997/01/10 00:52	01/10 05:00	01/11 03:00	MC (S–N)	Wind	−15.8	456.9	11.8	−7.2	−18.3	−78
2	1997/05/15 01:16	05/15 09:50	05/15 23:20	MC (S–N)	Wind	−25.5	434.6	10.5	−11.1	−22.6	−115
3	1997/12/10 04:33	12/10 18:40	12/11 10:20	MC (S)	Wind	−13.4	347.3	15.7	−4.7	−19.7	−60
4	1999/04/16 10:35	04/16 22:00	04/17 19:00	MC (S–N)	ACE	−16.2	430.4	12.2	−7.0	−17.7	−91
5	1999/10/21 01:37	10/21 05:00	10/21 18:00	MC (N–S)	ACE	−16.1	437.2	9.7	−7.0	−8.5	−5
6	2000/01/22 00:23	01/22 06:00	01/23 02:00	MC (N–S)	ACE	−16.9	391.5	17.6	−6.6	−22.6	−97
7	2000/07/28 05:43	07/28 14:00	07/29 10:00	MC (N–S)	ACE	−12.6	464.9	12.9	−5.9	−13.7	−71
8	2000/08/11 18:11	08/12 05:00	08/13 06:00	MC (S–N)	ACE	−29.4	589.8	9.0	−17.3	−24.0	−235
9	2000/09/17 16:57	09/17 16:57	09/18 00:00	sheath	ACE	−36.2	688.0	3.4	−24.9	−13.8	−201
10	2000/10/12 21:45	10/13 16:30	10/14 14:00	MC (N–S)	ACE	−13.0	410.7	16.8	−5.3	−16.7	−107
11	2000/11/26 11:24	11/27 09:30	11/27 19:50	MC (S)	ACE	−9.0	603.9	8.7	−5.4	−6.0	−51
12	2001/03/22 12:42	03/23 04:00	03/23 14:40	MC (N–S)	ACE	−7.7	413.1	8.1	−3.2	−3.9	−75
13	2001/04/11 13:15	04/11 13:15	04/11 23:00	sheath	ACE	−33.4	756.2	6.0	−25.3	−17.7	−271
14	2001/10/11 16:19	10/11 16:19	10/12 03:30	sheath	ACE	−21.0	505.0	2.2	−10.6	−4.0	−70
15	2002/03/18 12:37	03/18 12:37	03/19 05:00	sheath	ACE	−16.8	432.7	2.4	−7.3	−3.9	−37
16	2002/04/17 10:21	04/18 01:00	04/19 10:00	MC (S–N)	ACE	−12.7	522.5	21.3	−6.6	−24.9	−127
17	2002/05/18 19:13	05/19 02:45	05/20 04:45	MC (S–N)	ACE	−12.3	471.4	5.2	−5.8	−4.9	−58
18	2002/07/17 15:25	07/17 15:25	07/18 10:30	sheath	ACE	−4.4	427.5	1.5	−1.9	−0.8	−17
19	2003/08/17 13:41	08/18 10:30	08/19 11:30	MC (S–N)	ACE	−17.2	457.9	17.7	−7.9	−32.4	−148
20	2004/07/24 05:38	07/24 17:30	07/25 06:30	MC (N–S)	ACE	−17.4	491.5	9.0	−8.5	−21.8	−106
21	2004/12/11 12:57	12/12 22:30	12/13 20:30	MC (S–N)	ACE	−13.6	401.2	4.4	−5.5	−4.1	−56

Table 1 (*Continued*)

Event	ICME shock year/mon/day UT	MC or sheath start mon/day UT	MC or sheath end mon/day UT	Type	S/C	B_{Smin} (nT)	$V_{B_{Smin}}$ (km s^{-1})	T_{B_S} (hour)	$Ey_{B_{Smin}}$ (mV m)	$\int V_{SW} \times B_S\,dt$ (V m s)	Dst_{min} (nT)
22	2005/05/15 02:11	05/15 06:00	05/16 04:00	MC (S–N)	ACE	−48.0	928.9	7.5	−44.6	−22.8	−247
23	2005/05/20 03:15	05/20 15:10	05/21 06:10	MC (N–S)	ACE	−7.9	412.6	4.9	−3.3	−3.5	−63
24	2005/07/10 02:47	07/10 17:00	07/11 00:00	MC (S–N)	ACE	−15.2	472.3	6.8	−7.2	−8.6	−92
25	2006/08/19 10:51	08/19 16:45	08/19 23:45	MC (S)	ACE	−12.6	402.4	6.6	−5.1	−8.9	−79

Columns 2–4: ICME-driven shock arrival, MC or sheath start and end times. Column 5: Geoeffective ICME substructure. Magnetic field rotation of an ICME in B_S in parentheses. S–N (N–S) indicates that B_Z rotated from southward (northward) to northward (southward). S represents that B_S is mostly southward. Column 6: Observing satellite of an ICME. Columns 7–11: the minimum value of a southward magnetic field, solar wind speed at minimum southward magnetic field, duration of southward magnetic field, convection electric field, and solar wind energy proxy. Column 12: the minimum value of the Dst index for a geomagnetic disturbance caused by an ICME.

Table 2 Geometrical parameters of 25 ICMEs derived from the linear force-free toroidal flux-rope fitting model.

Event	R_M (AU)	r_{m0} (AU)	θ_n (°)	ϕ_n (°)	sgn B_X +/-	P_Y (r_{m0})	P_Z (r_{m0})	d_{min} (r_{m0})	Impact location (Eastern/Western)
1	0.62	0.064	16.8	123.9	−	−0.12	−0.27	0.22	Eastern
2	0.15	0.036	−20.0	60.0	−	−0.23	−0.28	0.30	Western
3	0.30	0.02	−76.5	116.4	+	0.48	−0.69	0.64	Eastern
4	0.40	0.055	−20.0	55.0	−	−0.51	0.24	0.06	Western
5	0.29	0.067	−29.5	101.5	+	−0.23	0.95	0.90	Eastern
6	0.20	0.048	−71.5	352.9	−	−0.68	−0.03	0.70	Western
7	0.20	0.025	−36.6	78.5	+	−0.03	−0.51	0.11	Eastern
8	0.29	0.033	−19.7	283.1	+	−0.52	1.08	0.73	Eastern
9	(Sheath-storm event) Flux-rope fitting is not applicable								
10	0.37	0.037	−55.9	263.1	−	0.82	0.38	0.57	Western
11	0.30	0.018	−11.5	262.8	+	0.26	−0.69	0.58	Eastern
12	0.25	0.064	55.0	85.1	−	0.19	−0.95	0.94	Eastern
13	(Sheath-storm event) Flux-rope fitting is not applicable								
14	(Sheath-storm event) Flux-rope fitting is not applicable								
15	(Sheath-storm event) Flux-rope fitting is not applicable								
16	0.52	0.114	74.0	20.0	+	0.24	1.16	0.69	Western
17	0.30	0.034	41.6	117.2	−	−1.02	0.35	0.61	Eastern
18	(Sheath-storm event) Flux-rope fitting is not applicable								
19	0.52	0.078	40.0	50.0	+	0.27	0.54	0.27	Western
20	0.38	0.048	62.0	223.6	−	−0.45	1.19	0.55	Eastern
21	0.35	0.029	−55.6	98.8	+	−0.86	0.49	0.57	Eastern
22	0.44	0.026	−81.6	235.6	−	0.63	−0.08	0.21	Western
23	0.22	0.018	−29.5	107.0	−	0.43	0.83	0.78	Western
24	0.10	0.012	−23.5	80.9	−	−0.56	−0.29	0.48	Western
25	0.08	0.012	72.5	95.1	−	0.35	0.58	0.63	Eastern

Columns 2 and 3: the major and minor radii of an MC, which indicate the curvature radius and thickness of the MC, respectively. Columns 4 and 5: the latitude and longitude angles of a vector normal to the MC plane defined by the axial magnetic field. If the latitude is 90°, the MC plane is parallel to the Sun–Earth plane and the latitude is 0°, the MC plane is perpendicular to the Sun–Earth plane. Column 6: the sign of the B_X component of the axial field on the side of the MC where the spacecraft encounters the MC. Columns 7–9: the position in the Y–Z plane ($X = 0$) of the spacecraft track from the MC axis, and the smallest distance from the torus axis to the spacecraft during the MC passage. Column 10: which flank of an ICME encountered the Earth. Eastern (Western) indicates that the eastern (western) flank of an ICME encountered the Earth.

pacts the spacecraft. We define this kind of event as a western flank event. Since the toroidal flux-rope fitting model is not applicable to the five sheath events, we can only estimate the impact locations of 20 MCs with southward magnetic fields. The impact locations of the 20 MCs are presented in column 9 of Table 2. It should be noted that relative position of the Earth trajectory from the ICME axis in the Y or Z components of GSE coordinate (P_Y or P_Z) values greater than 1 in the columns 7–8 of Table 2 do not necessarily mean that the spacecraft missed the MCs, d_{min} values less than 1 in the column 9 of Table 2 indicate that the MCs were intersected by the spacecraft. It should be noted that $\sqrt{P_Y^2 + P_Z^2} \geq 1$ (circle of radius 1) in Figures 6 and 7 do not necessarily mean that the spacecraft missed the cloud, and that $\sqrt{P_Y^2 + P_Z^2}$ is not the same as d_{min}.
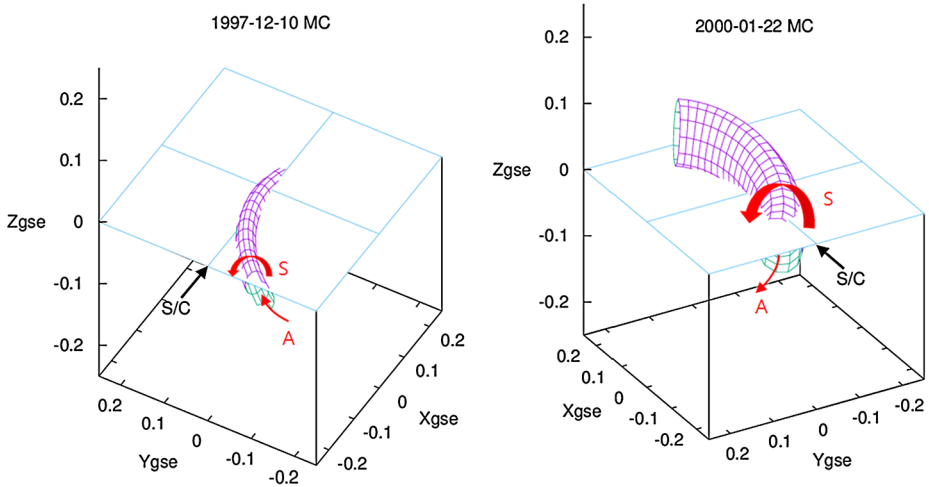
Figure 2   3D geometries of ICMEs for 10 December 1997 (*left*, event No. 3 in Table 1) and 22 January 2000 (*right*, event No. 6 in Table 1) estimated by the toroidal fitting model. S/C indicated with *black arrow*, S with *red curved arrow*, and A with *red half circle arrow* represent the direction of spacecraft trajectory relative to the ICME, magnetic field on the surface, and axial field, respectively.

2.2. Analysis

We make a simple linear regression analysis to find the relationship between Dst index and solar wind conditions of ICMEs. The slope of the linear regression equation for each parameter indicates the efficiency in the generation of a geomagnetic storm. We make the same analysis by dividing ICMEs into two subgroups according to their geoeffective ICME substructures (MC-associated storm and sheath-associated storm events). We also examine the dependence of the geomagnetic storms on the combination of ICME–Earth impact geometrical parameters such as the following: eastern flank and positive value of P_Y (E + P_{Y+}), eastern flank and negative value of P_Y (E + P_{Y-}), western flank and positive value of P_Y (W + P_{Y+}), and western flank and negative value of P_Y (W + P_{Y-}) as shown in Figure 3. Here P_Y indicates the relative position of the spacecraft (or Earth) trajectory from the ICME axis in the Y component of GSE coordinate. If P_Y is negative (or positive) in an eastern flank event, the spacecraft passes the inner (or outer) edge of eastern flank of an ICME. If P_Y is negative (or positive) in a western flank event, the spacecraft passes the outer (or inner) edge of western flank of an ICME.

3. Results and Discussion

3.1. Dependence of Geomagnetic Storms on ICME Solar Wind Conditions

Figure 4 shows the relationship between the minimum Dst index (Dst$_{min}$) and solar wind conditions of 25 ICMEs: minimum southward magnetic field (B_{Smin}), solar wind speed at B_{Smin} ($V_{B_{Smin}}$), southward magnetic field duration (T_{B_S}), convection electric field ($E_{Y_{B_{Smin}}} = V_{B_{Smin}} \times B_{Smin}$), and solar wind energy proxy ($\int V_{SW} \times B_S \, dt$). As shown in Figure 4, all of the solar wind conditions except for T_{B_S} have high correlation coefficients (CC) with
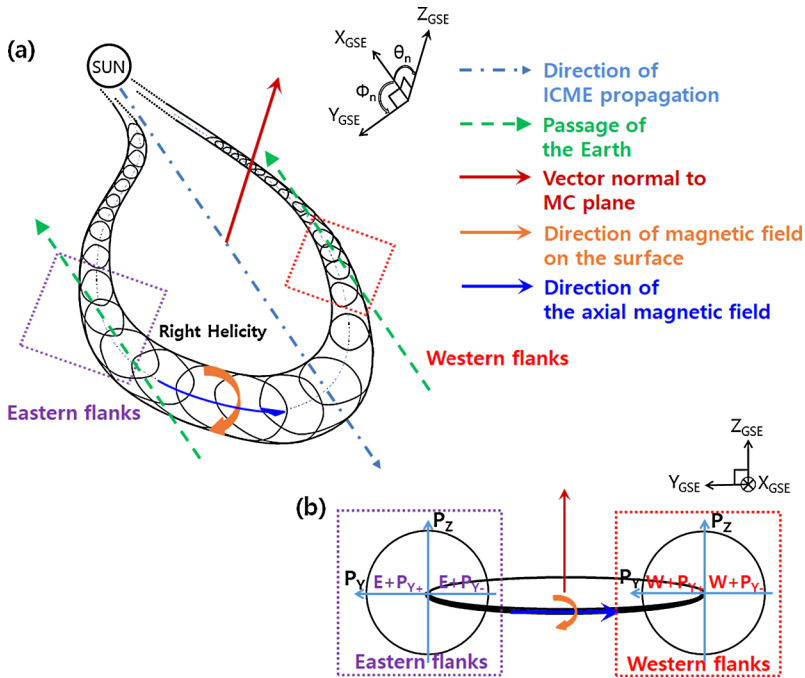
Figure 3 Cartoons showing (**a**) the ICME–Earth impact geometry and (**b**) the combination of ICME–Earth impact geometrical parameters in $Y-Z$ plane ($X = 0$) for a special case ($\theta_n = 90°$ and $\phi_n = 0°$), which means that a MC plane is in the Sun–Earth plane ($X-Y$ plane) and a vector normal to the MC plane is in the Z direction of the GSE coordinate. The *dotted boxes* indicate areas where cross sections of MCs deduced from torus fitting model are shown.

statistical significance (SS) with the Dst index: CC = 0.83 with SS = 99.99% for B_{Smin}, CC = 0.82 with SS = 99.99% for $E_{Y_{B_{Smin}}}$, CC = -0.78 with SS = 99.99% for $V_{B_{Smin}}$, CC = 0.61 with SS = 99.90% for $\int V_{SW} \times B_S \, dt$, and CC = -0.19 with SS = 33.03% for T_{B_S}. Here the statistical significance (SS) is defined as $(1 - \text{p-value}) \times 100$. The p-value, which is the probability to accept the null hypothesis that both quantities are randomly distributed, is estimated by using the number of data and the correlation coefficient under the assumption of Student's t cumulative-distribution function (Neter *et al.*, 1996). For example, if the p-value is less than 0.0001, SS is about 99.99%. When we use maximum solar wind speed (V_{max}) during ICME passages with B_S at the time of V_{max} ($B_{S_{Vmax}}$), we obtain a similar statistical trend: CC = -0.77 with SS = 99.99% for V_{max}, CC = 0.67 with SS = 99.99% for $E_{Y_{Vmax}}$, and CC = 0.56 with SS = 99.70% for $B_{S_{Vmax}}$. Our results of the relationships between Dst_{min} and B_{Smin} (or $E_{Y_{B_{Smin}}}$) are consistent with previous ones (Echer *et al.*, 2008; Richardson and Cane, 2010). By investigating 300 ICME–storm pairs from 1996 to 2009, Richardson and Cane (2010) obtained a similar statistical trend: B_{Smin} and $E_{Y_{Vmax}}$ were well correlated with the Dst index (CC = 0.89 with SS = 99.99% for B_{Smin} and CC = 0.90 with SS = 99.99% for $E_{Y_{Vmax}}$). Echer *et al.* (2008) analyzed 90 ICME–intense storm pairs and found that a slightly lower dependence of Dst index on the B_{Smin} or E_{Ymax}: CC = 0.80 with SS = 99.99% for B_{Smin} and CC = 0.84 with SS = 99.99% for E_{Ymax}. In this study, we note that $V_{B_{Smin}}$ has a high correlation (CC = -0.78 with SS = 99.99%) with Dst index and $V_{B_{Smin}}$ is well correlated with B_{Smin} (CC = -0.81 with SS = 99.99%), which are different from the previous one: CC and SS of V_{max} and Dst index = -0.54 and 99.99%, and CC and SS of
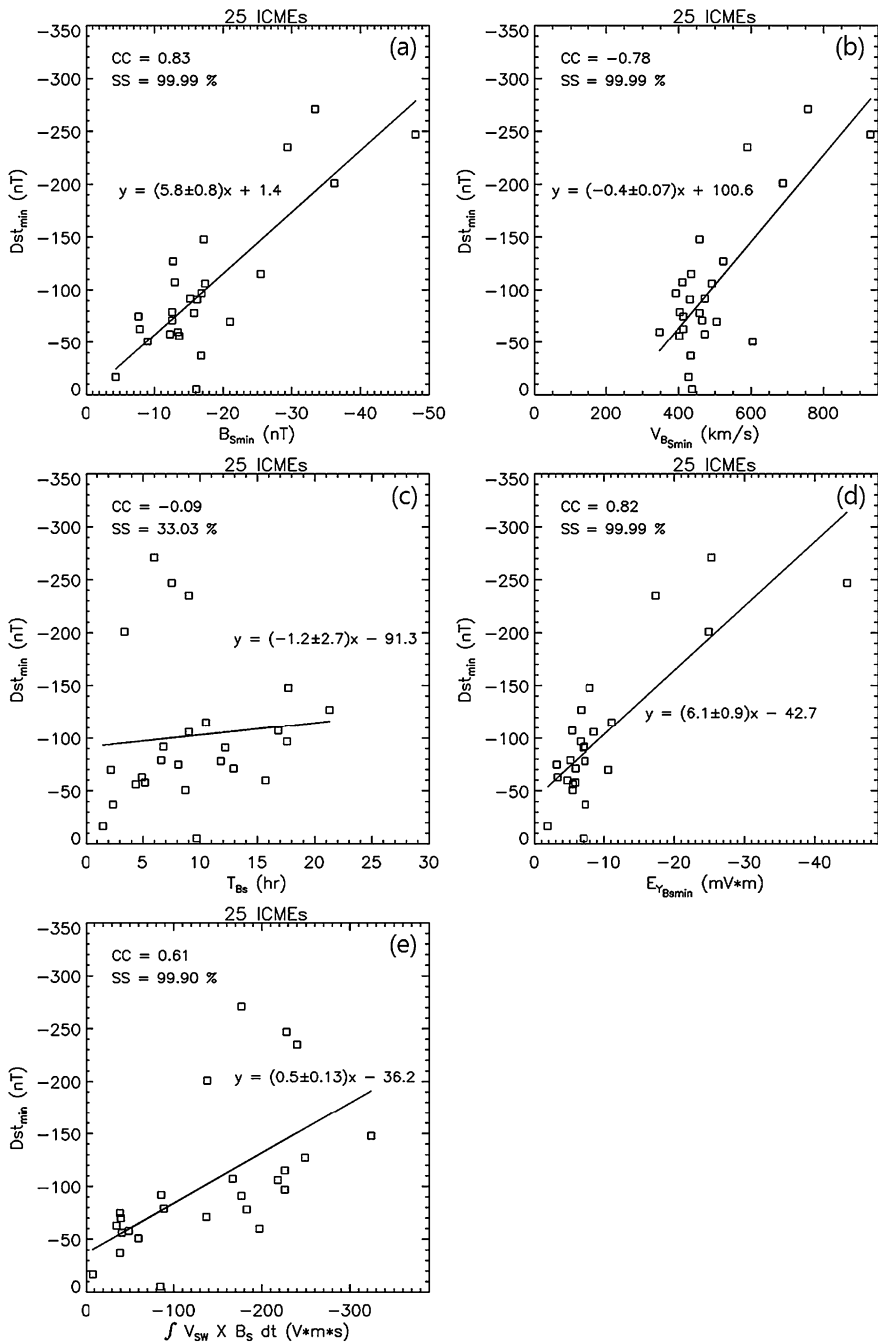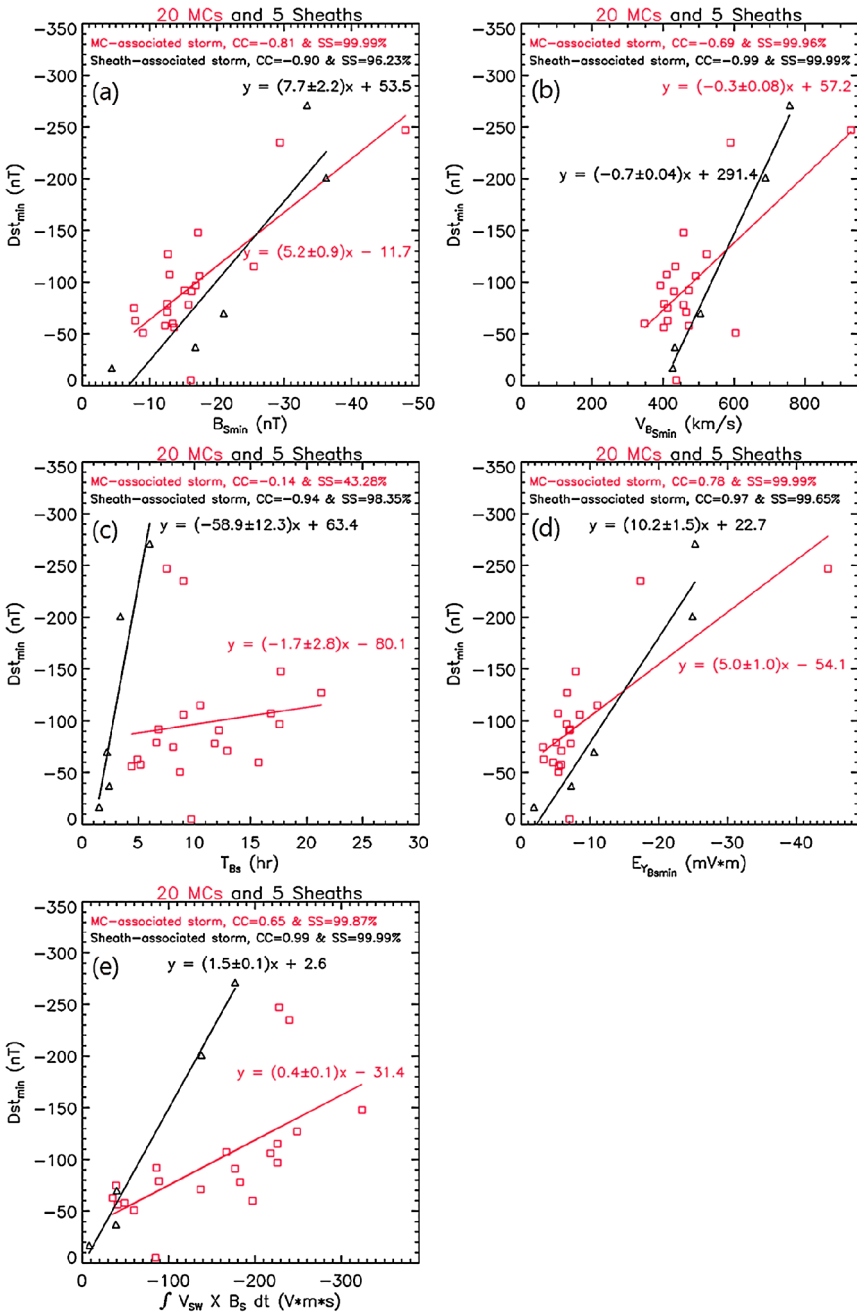
Figure 4 Scatter plots between minimum Dst index (Dst_{min}) and solar wind conditions of ICMEs: (**a**) minimum southward magnetic field (B_{Smin}), (**b**) solar wind speed (V_{SW}) at B_{Smin} ($V_{B_{Smin}}$), (**c**) southward magnetic field duration (T_{B_S}), (**d**) convection electric field ($E_{Y_{B_{Smin}}} = V_{B_{Smin}} \times B_{Smin}$), and (**e**) solar wind energy proxy ($\int V_{SW} \times B_S \, dt$). The *solid line* is a linear fit to all of the data points. CC and SS indicate correlation coefficient and statistical significance, respectively.

V_{max} and $B_{\text{Smean}} = -0.22$ and 99.99% by Richardson and Cane (2010). To test whether the two correlation coefficients are significantly different from each other, we use Fisher's r-to-z transformation and calculate a probability value (P_{Fisher}). P_{Fisher} of less than 0.05 indicates that the two correlation coefficients are significantly different from each other. When we compare statistical results from our analysis and that of Richardson and Cane (2010), we find differences between two correlation coefficients: $P_{\text{Fisher}} = 0.046$ for solar wind speed and Dst index, and $P_{\text{Fisher}} = 0.000043$ for solar wind speed and southward magnetic field strength. Our results might indirectly suggest that the compression at the leading edge of an ICME during its propagation cause an increase in the southward magnetic field of the ICME (Lindsay *et al.*, 1999; Yurchyshyn, Wang, and Abramenko, 2004; Gopalswamy, 2008). Our findings together with the previous ones support the idea that the southward magnetic field and convection electric field are key drivers in generating geomagnetic disturbances.

Since observational solar wind conditions of MCs often become complex due to interaction between an ICME and another ICME (or solar wind) during ICME passages, the determination of MC boundaries can be subjective. This may cause different results of the relationship between Dst index and solar wind conditions and also different flux-rope properties, 3D geometrical parameters, according to the various definitions of the MC boundaries. To examine this possibility, we compare the relationships using our selected MC boundaries shown in Table 1 with those from Table 1 of Richardson and Cane (2010). For this purpose, we select 12 ICME–storm events whose shock arrival times and geomagnetic storms are similar to each other: the difference of shock arrival times is less than 1 h and relative difference of Dst index, defined as the difference of Dst index between our data set and those from Richardson and Cane (2010) divided by the Dst index determined by us, is less than 0.1 (10%). From this analysis, we find that the relationships (CC = 0.85 with SS = 99.98% for B_{Smin}, CC = -0.84 with SS = 99.98% for $V_{B_{\text{Smin}}}$, CC = -0.12 with SS = 28.25% for $T_{B_{\text{S}}}$, CC = 0.82 with SS = 99.95% for $E_{Y_{B_{\text{Smin}}}}$, and CC = 0.55 with SS = 93.64% for $\int V_{\text{SW}} \times B_{\text{S}}\, dt$) using our selected MC boundaries are similar to those using the MC boundaries by Richardson and Cane (2010): CC = 0.88 with SS = 99.99% for B_{Smin}, CC = -0.84 with SS = 99.98% for $V_{B_{\text{Smin}}}$, CC = -0.35 with SS = 72.71% for $T_{B_{\text{S}}}$, CC = 0.82 with SS = 99.95% for $E_{Y_{B_{\text{Smin}}}}$, and CC = 0.56 with SS = 94.24% for $\int V_{\text{SW}} \times B_{\text{S}}\, dt$. Regarding the difference of 3D geometrical parameters by using different MC boundaries, Marubashi *et al.* (2016) performed a magnetic flux-rope fitting analysis with two MC boundaries. They applied the toroidal magnetic flux-rope model to an MC observed on 17 March 2015 with two different MC intervals, and showed that the difference is small enough to maintain impact location of the ICME at Earth and the relative position of the Earth trajectory as shown in Table A2 and Figure A1 of Appendix of Marubashi *et al.* (2016). We also find a similar statistical trend when we use small changes (within about 2 h) in the start/end times of MCs. Therefore, our results are not expected to be very different from those using other MC boundaries.

3.2. Dependence of Geomagnetic Storms on ICME Geoeffective Substructures

To examine the dependence of Dst_{min} on the geoeffective substructures of ICMEs, we divide 25 storms into two groups: 20 MC-associated storm and five sheath-associated storm events. Figure 5 shows the relationship between Dst_{min} and solar wind conditions of MC-associated storm (red square symbols) and sheath-associated storm events (black triangle symbols). For 20 MC-associated storms as shown in Figure 5, the minimum southward magnetic field (B_{Smin}) and convection electric field ($E_{Y_{B_{\text{Smin}}}}$) have higher correlation coefficients with Dst index than the other parameters: CC = 0.81 with SS = 99.99% for B_{Smin}, CC = 0.78
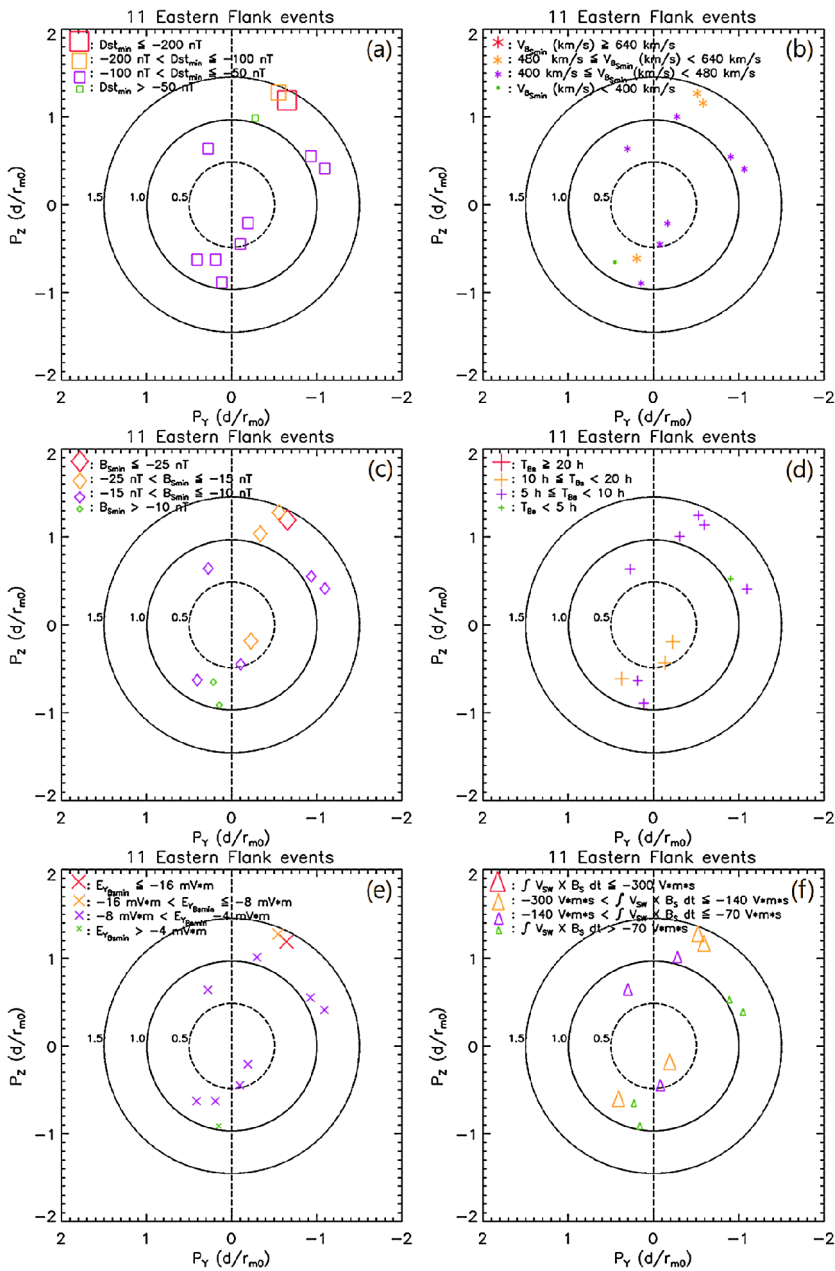
Figure 5 Scatter plots between minimum Dst index (Dst_{min}) and solar wind conditions of ICME sub-structures (MCs and sheaths): (**a**) minimum southward magnetic field (B_{Smin}), (**b**) solar wind speed (V_{SW}) at B_{Smin} ($V_{B_{Smin}}$), (**c**) southward magnetic field duration (T_{B_S}), (**d**) convection electric field ($E_{Y_{B_{Smin}}} = V_{B_{Smin}} \times B_{Smin}$), and (**e**) solar wind energy proxy ($\int V_{SW} \times B_S \, dt$). *Red square* and *black tri-angle* symbols represent solar wind conditions for MC-associated storm and sheath-associated storm events, respectively. The *solid lines*, CC, and SS are the same as in Figure 4.

with SS $= 99.99\%$ for $E_{Y_{B_{\mathrm{Smin}}}}$, CC $= -0.69$ with SS $= 99.96\%$ for $V_{B_{\mathrm{Smin}}}$, CC $= 0.65$ with SS $= 99.87\%$ for $\int V_{\mathrm{SW}} \times B_{\mathrm{S}} \, dt$, and CC $= -0.14$ with SS $= 43.28\%$ for $T_{B_{\mathrm{S}}}$. For the five sheath-associated storms as shown in Figure 5, all of solar wind conditions except have high correlation coefficients with statistical significance: CC $= 0.90$ with SS $= 96.23\%$ for B_{Smin}, CC $= 0.97$ with SS $= 99.65\%$ for $E_{Y_{B_{\mathrm{Smin}}}}$, CC $= -0.99$ with SS $= 99.99\%$ for $V_{B_{\mathrm{Smin}}}$, CC $= 0.99$ with SS $= 99.99\%$ for $\int V_{\mathrm{SW}} \times B_{\mathrm{S}} \, dt$, and CC $= -0.94$ with SS $= 98.35\%$ for $T_{B_{\mathrm{S}}}$. Our results of the relationships between $\mathrm{Dst_{min}}$ and B_{Smin} (or $E_{Y_{B_{\mathrm{Smin}}}}$) are consistent with previous results obtained by Gopalswamy (2008) who examined 50 MC-storms and 59 sheath-storms and found that B_{Smin} and $E_{Y_{V\mathrm{mean}}}$ were well correlated with the Dst index in both events: In MC-storm (sheath-storm) events, CC $= 0.79$ with SS $= 99.99\%$ (CC $= 0.77$ with SS $= 99.99\%$) for B_{Smin} and CC $= 0.90$ with SS $= 99.99\%$ (CC $= 0.86$ with SS $= 99.99\%$) for $E_{Y_{V\mathrm{mean}}}$. In this study, we note that correlation coefficients of solar wind conditions in a sheath with the Dst index are higher than those in MC; for $E_{Y_{B_{\mathrm{Smin}}}}$, CC $= 0.97$ with SS $= 99.65\%$ in sheath and CC $= 0.78$ with SS $= 99.99\%$ in MC. When we test the significance of the difference in two correlations by using Fisher's r to z transformation, there are no differences between them: the probability value (P_{Fisher}) $= 0.16$, which might be caused by usage of limited data sampling for the sheath events. We also find that all slopes of linear regression lines for sheath-storm events are steeper (≥ 1.4) than those of the MC-storm events in the relationship between $\mathrm{Dst_{min}}$ and solar wind conditions as shown in Figure 5, implying that sheaths can produce stronger storms than MCs for given solar wind conditions. This result is consistent with a previous one by Yermolaev *et al.* (2010) who analyzed 798 magnetic storms with Dst < -50 nT by using the method of superposed epoch analysis. They found that at equal values of time integrated B_{S} or ($E_Y = V_{\mathrm{SW}} \times B_{\mathrm{S}}$) during MC and sheath passages the sheath-associated storm is larger than MC-associated storm (Figure 9 of Yermolaev *et al.*, 2010). The above results are explained by the efficiency dependence on the plasma density in the tail coming from solar wind density (Terasawa *et al.*, 1997; Ebihara and Ejiri, 2000; Keika, Ebihara, and Kataoka, 2015) or caused by different general solar wind conditions between sheaths and MCs: sheaths have a higher density, dynamic and thermal pressures, and temperature with a higher fluctuation of the parameters and magnetic fields than MCs (Yermolaev *et al.*, 2012). However, we need a larger sample of the events to confirm this speculation.

3.3. Dependence of Geomagnetic Storms on 3D ICME–Earth Impact Geometries

We conduct a statistical investigation to find whether or not geomagnetic storms depend on ICME–Earth impact geometrical parameters: impact location of the ICME at the Earth and relative position of the Earth trajectory from the ICME axis in the Y–Z plane of the GSE coordinate system. For this purpose, we use 20 MC-associated storm events and classify them into two subgroups according to which flank of a ICME encounters the Earth: 11 eastern flank events and 9 western flank events. Figures 6 and 7 show distributions of geomagnetic disturbances and solar wind conditions on the relative positions for 11 eastern flank events and nine western flank events, respectively.

For the 11 eastern flank events as shown in Figure 6(a), 64% (7/11) of storms and 100% (2/2) of major storms ($\mathrm{Dst_{min}} \leq -100$ nT) occur in the regions at negative P_Y (E $+ P_{Y-}$). We also have examined the dependence of ICME solar wind conditions on 3D ICME–Earth impact geometries. We find similar statistical trends: 66% (2/3) of fast solar wind speeds ($V_{B_{\mathrm{Smin}}} \geq 480 \mathrm{\ km\,s^{-1}}$), 100% (4/4) of intense southward magnetic fields ($B_{\mathrm{Smin}} \leq -15$ nT), 66% (2/3) of long southward magnetic field durations ($T_{B_{\mathrm{S}}} \geq 10$ hr), 100% (2/2) of intense electric fields ($E_{Y_{B_{\mathrm{Smin}}}} \leq -8 \mathrm{\ mV\,m}$), and 75% (3/4) of intense solar wind energy proxies

Figure 6 Scatter plots of geomagnetic storm index and solar wind conditions at the relative position of the spacecraft track and the MC axis for 11 eastern flank events: (**a**) minimum Dst index (Dst_{min}) (*square symbols*), (**b**) solar wind speed (V_{SW}) at B_{Smin} ($V_{B_{Smin}}$) (*star symbols*), (**c**) minimum southward magnetic field (B_{Smin}) (*diamond symbols*), (**d**) southward magnetic field duration (T_{B_S}) (*plus symbols*), (**e**) convection electric field ($E_{Y_{B_{Smin}}} = V_{B_{Smin}} \times B_{Smin}$) (*cross symbols*), and (**f**) solar wind energy proxy ($\int V_{SW} \times B_S \, dt$) (*triangle symbols*). Here, the relative position is presented in the Y–Z plane of the GSE coordinate system. Symbol sizes are related to intensities of each of the parameters. The *vertical dashed line* and *circle* of radius 1 indicate that we have a zero value of P_Y and that it is near the surface of an MC, respectively.
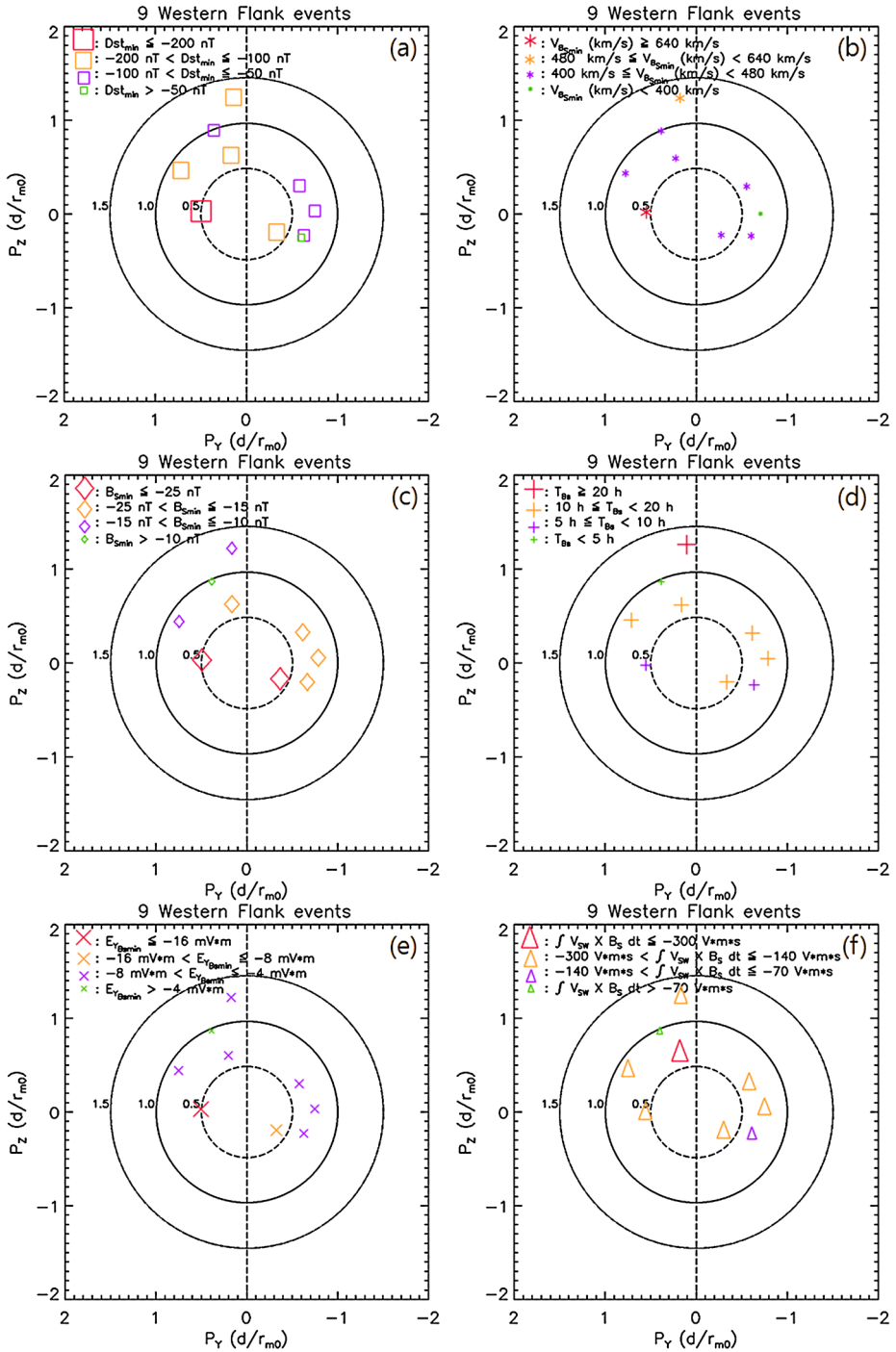
Figure 7 Same as Figure 6, but for the nine western flank magnetic clouds.

($\int V_{SW} \times B_S \, dt \leq -140$ V m s) occur in the E $+ P_{Y-}$ region as shown in Figure 6(b), (c), (d), (e), and (f). For eastern flank events, we suggest that the dependence of geomagnetic storms on 3D ICME–Earth impact geometries is caused by asymmetric distributions of geo-effective solar wind conditions. Especially, the asymmetric southward magnetic field distributions, intense magnetic fields are located in the near inner edge of MCs, are expected based on toroidal linear force-free magnetic flux-rope modeling (Romashets and Vandas, 2013; Vandas and Romashets, 2016).

For the nine western flank events as shown in Figure 7, 56% (5/9) of storms and 80% (4/5) of major storms occur in positive P_Y regions for the western flank events (W $+ P_{Y+}$) as shown in Figure 7(a). We find that 100% (2/2) of fast solar wind speeds ($V_{B_{Smin}} \geq 480$ km s^{-1}), 33% (2/6) of intense southward magnetic fields ($B_{Smin} \leq -15$ nT), 50% (3/6) of long southward magnetic field durations ($T_{B_S} \geq 10$ hr), 50% (1/2) of intense electric fields ($E_{Y_{B_{Smin}}} \leq -8$ mV m), and 57% (4/7) of intense solar wind energy proxies ($\int V_{SW} \times B_S \, dt \leq -140$ V m s) occur in the W $+ P_{Y+}$ region as shown in Figure 7(b), (c), (d), (e), and (f). We note that, even though many major storms occurred in the near inner edges of MCs, geoeffective solar wind conditions are not located in the inner edges of MCs. These results are a little bit different from those from the eastern flank events. From our results for the western flank events, we suggest that the strength of a geomagnetic storm depends on the ICME–Earth impact geometries, while it is independent of the other geoeffective parameters.

Recently, Wu *et al.* (2017) investigated the dependence of geomagnetic storm strengths on MC types by using 217 MCs observed by *Wind* from 1995 to 2015. To do this, they divided MCs into two types: 1) N–S type, B rotated from northward to southward and 2) S–N type, B rotated from southward to northward. They found that the average storm strength (-107 nT) of S–N type is larger than that (-79 nT) of N–S type. When we use our data set, we find similar results: -110 nT for S–N type and -75 nT for N–S type. These tendencies might present a bias against the results of the dependence of geomagnetic storms on 3D ICME–Earth impact geometries. To exclude this possibility, we use 13 MCs with S–N type and examine whether or not the strength of a geomagnetic storm depends on the ICME–Earth impact geometries. We find the following results. For seven eastern flank events, 57% (4/7) of storms and 100% (1/1) of major storms occur in the E $+ P_{Y-}$ region. We also find similar statistical trends in solar wind parameters: 100% (2/2) of intense southward magnetic fields, 100% (1/1) of intense electric fields, 50% (1/2) of long southward magnetic field durations, 66% (2/3) of intense solar wind energy proxies occur in the E $+ P_{Y-}$ region. For six western flank events, 50% (3/6) of storms and 75% (3/4) of major storms occur in the W $+ P_{Y+}$ region. We find that 40% (2/5) of intense southward magnetic fields, 50% (1/2) of intense electric fields, 50% (2/4) of long southward magnetic field durations, and 60% (3/5) of intense solar wind energy proxies occur in the W $+ P_{Y+}$ region. Therefore, we think that the strength of a geomagnetic storm is dependent on the geometrical impact parameter for the western flank events. It should be noted that it is hard to determine conclusively whether or not Dst index is dependent on the geometrical impact parameter because we only use 20 MCs (11 eastern and nine western flank events). Therefore, we need more samples of the events to confirm this speculation.

4. Summary and Conclusions

In this study, we have investigated the relationship between minimum Dst index (Dst$_{min}$) and solar wind conditions of ICMEs (minimum southward magnetic field (B_{Smin}), solar

wind speed (V_{SW}) at B_{Smin} ($V_{B_{\text{Smin}}}$), southward magnetic field duration ($T_{B_{\text{S}}}$), convection electric field ($E_{Y_{B_{\text{Smin}}}} = V_{B_{\text{Smin}}} \times B_{\text{Smin}}$), and solar wind energy proxy ($\int V_{\text{SW}} \times B_{\text{S}}\, dt$)) in order to determine the key solar wind parameter for generating a geomagnetic storm. We also have examined the dependence of geomagnetic storms on both geoeffective ICME sub-structures (magnetic clouds (MCs) and the compression regions ahead of the MCs (sheaths)) and ICME–Earth impact geometries (impact location of the ICME at the Earth and relative position of the Earth trajectory (P_Y and P_Z) from the ICME axis in the $Y-Z$ plane) derived from the linear force-free toroidal flux-rope model. For this purpose, we use 25 ICME–storm pairs during Solar Cycle 23 that are available by the toroidal fitting model and their associated geomagnetic storms are well identified.

The main results of this study can be summarized as follows. First, all solar wind parameters have relatively high correlation coefficients (CC) with the storm strength (CC ≥ 0.6), except $T_{B_{\text{S}}}$ (CC < 0.1). Second, all slopes of linear regression lines for sheath-storm events are steeper (≥ 1.4) than those of the MC-storm events in the relationship between Dst_{min} and solar wind conditions, implying that efficiency of sheath for the process of geomagnetic storm generation is higher than that of MC. These results suggest that different general solar wind conditions, such as sheaths having a higher density, and higher dynamic and thermal pressures with a higher fluctuation of the parameters and magnetic fields than MCs, have higher impact on geomagnetic storm generation. Third, regarding the geometric encounter of ICME with Earth, we find that 64% (7/11) of storms and 100% (2/2) of major storms ($\text{Dst}_{\text{min}} \leq -100$ nT) occur in the regions at negative P_Y for the Eastern flank events. We find similar statistical trends in solar wind conditions, suggesting that the dependence of geomagnetic storms on 3D ICME–Earth impact geometries is caused by asymmetric distributions of geoeffective solar wind conditions. In particular, the asymmetric southward magnetic field distributions and intense magnetic fields are located in the near inner edge of MCs, as expected based on toroidal linear force-free magnetic flux-rope modeling. For nine western flank events, 56% (5/9) of storms and 80% (4/5) of major storms occur in positive P_Y regions while intense geoeffective solar wind conditions are not located in the inner edges of MCs. These results suggest that the strength of a geomagnetic storm depends on the ICME–Earth impact geometries as it determines the solar wind conditions at Earth. In summary, our results demonstrate that geoeffective solar wind conditions (B_{Smin} and $E_{Y_{B_{\text{Smin}}}}$) control the strength of geomagnetic storms, but the control changes depending on the ICME substructures (MCs and sheaths) and the ICME–Earth impact geometries (impact location of the ICME at the Earth and P_Y on ICME–Earth trajectory).

References

Bothmer, V., Schwenn, R.: 1998, *Ann. Geophys.* **16**, 1. DOI.

Bothmer, V., Rust, D.M.: 1997, *AGU Geophysical Monograph* **99**, 139. DOI.

Burlaga, L.F.: 1988, *J. Geophys. Res.* **93**, 7217. DOI.

Burlaga, L., Sittler, E., Mariani, F., Schwenn, R.: 1981, *J. Geophys. Res.* **86**, 6673. DOI.

Cho, K.-S., Park, S.-H., Marubashi, K., Gopalswamy, N., Akiyama, S., Yashiro, S., Kim, R.-S., Lim, E.-K.: 2013, *Solar Phys.* **284**, 105. DOI.

Cho, K.-S., Marubashi, K., Kim, R.-S., Park, S.-H., Lim, E.-K., Kim, S.-J., Kumar, P., Yurchyshyn, V., Moon, Y.-J., Lee, J.-O.: 2017, *J. Korean Astron. Soc.* **50**, 29. DOI.

Dungey, J.W.: 1961, *Phys. Rev. Lett.* **6**, 47. DOI.

Ebihara, Y., Ejiri, M.: 2000, *J. Geophys. Res. A* **105**, 15843. DOI.

Echer, E., Tsurutani, B.T., Gonzalez, W.D.: 2013, *J. Geophys. Res. A* **118**, 385. DOI.

Echer, E., Gonzalez, W.D., Tsurutani, B.T., Gonzalez, A.L.C.: 2008, *J. Geophys. Res. A* **113**, A05221. DOI.

Goldstein, H.: 1983, *NASA Conference Publication* **228**.

Gonzalez, W.D., Joselyn, J.A., Kamide, Y., Kroehl, H.W., Rostoker, G., Tsurutani, B.T., Vasyliunas, V.M.: 1994, *J. Geophys. Res.* **99**, 5771. DOI.

Gonzalez, W.D., Echer, E., Clua-Gonzalez, A.L., Tsurutani, B.T.: 2007, *Geophys. Res. Lett.* **34**, L06101. DOI.

Gonzalez, W.D., Echer, E., Tsurutani, B.T., Clúa de Gonzalez, A.L., Dal Lago, A.: 2011, *Space Sci. Rev.* **158**, 69. DOI.

Gopalswamy, N.: 2008, *J. Atmos. Solar-Terr. Phys.* **70**, 2078. DOI.

Gopalswamy, N., Xie, H., Mäkelä, P., Akiyama, S., Yashiro, S., Kaiser, M.L., Howard, R.A., Bougeret, J.-L.: 2010, *Astrophys. J.* **710**, 1111. DOI.

Huttunen, K., Koskinen, H.: 2004, *Ann. Geophys.* **22**, 1729. DOI.

Keika, V., Ebihara, Y., Kataoka, R.: 2015, *Earth Planets Space* **67**, 65. DOI.

Kim, R.-S., Cho, K.-S., Moon, Y.-J., Dryer, M., Lee, J., Yi, Y., Kim, K.-H., Wang, H., Park, Y.-D., Kim, Y.H.: 2010, *J. Geophys. Res. A* **115**, A12108. DOI.

Klein, L.W., Burlaga, L.F.: 1982, *J. Geophys. Res.* **87**, 613. DOI.

Lee, J.-O., Moon, Y.-J., Lee, K.-S., Kim, R.-S.: 2014, *Solar Phys.* **289**, 2233. DOI.

Lepping, R.P., Burlaga, L.F., Jones, J.A.: 1990, *J. Geophys. Res.* **95**, 11957. DOI.

Lindsay, G.M., Luhmann, J.G., Russell, C.T., Gosling, J.T.: 1999, *J. Geophys. Res.* **104**, 12515. DOI.

Marubashi, K.: 1986, *Adv. Space Res.* **6**, 335. DOI.

Marubashi, K., Lepping, R.P.: 2007, *Ann. Geophys.* **25**, 2453. DOI.

Marubashi, K., Cho, K.-S., Kim, Y.-H., Park, Y.-D., Park, S.-H.: 2012, *J. Geophys. Res. A* **117**, A01101. DOI.

Marubashi, K., Akiyama, S., Yashiro, S., Gopalswamy, N., Cho, K.-S., Park, Y.-D.: 2015, *Solar Phys.* **290**, 1371. DOI.

Marubashi, K., Cho, K.-S., Kim, R.-S., Kim, S., Park, S.-H., Ishibashi, H.: 2016, *Earth Planets Space* **68**, 173. DOI.

Mulligan, T., Russell, C.T., Luhmann, J.G.: 1998, *Geophys. Res. Lett.* **25**, 2959. DOI.

Neter, J., Kutner, M.H., Wasserman, W., Nachtsheim, C.: 1996, *Applied Linear Statistical Models*, 4th edn. McGraw-Hill/Irwin, New York.

Richardson, I.G., Cane, H.V.: 2010, *Solar Phys.* **264**, 189. DOI.

Richardson, I.G., Cane, H.V.: 2012, *J. Space Weather Space Clim.* **2**, A01. DOI.

Romashets, E., Vandas, M.: 2013, *Solar Phys.* **284**, 235. DOI.

Sugiura, M., Kamei, T.: 1991, *IAGA Bull.* **40**, Publ. Off., Int. Serv. Geomagn. Indices, Saint-Maur-des-Fosses, France.

Terasawa, T., Fujimoto, M., Mukai, T., Shinohara, I., Saito, Y., Yamamoto, T., Machida, S., Kokubun, S., Lazarus, A.J., Steinberg, J.T., Lepping, R.P.: 1997, *Geophys. Res. Lett.* **24**, 935. DOI.

Vandas, M., Romashets, E.: 2016, *Astron. Astrophys.* **585**, A108. DOI.

Wu, C.-C., Lepping, R.P., Berdichevsky, D.B., Liou, K.: 2017, *Space Weather* **15**, 517. DOI.

Yermolaev, Y.I., Nikolaeva, N.S., Lodkina, I.G., Yermolaev, M.Y.: 2010, *Ann. Geophys.* **28**, 2177. DOI.

Yermolaev, Y.I., Nikolaeva, N.S., Lodkina, I.G., Yermolaev, M.Y.: 2012, *J. Geophys. Res. A* **117**, A00L07. DOI.

Yurchyshyn, V., Wang, H., Abramenko, V.: 2004, *Space Weather* **2**, S02001. DOI.

Zhang, J., Richardson, I.G., Webb, D.F., Gopalswamy, N., Huttunen, E., Kasper, J.C., Nitta, N.V., Poomvises, W., Thompson, B.J., Wu, C.-C., Yashiro, S., Zhukov, A.N.: 2007, *J. Geophys. Res. A* **112**, A10102. DOI.

Zhao, X., Hoeksema, J.T.: 1996, *J. Geophys. Res. A* **101**, 4825. DOI.